Robust topological edge states induced by latent mirror symmetry

Li-Yang Zheng [*], Yu-Fan Li, Jin Zhang, and Yongsheng Huang[†]

School of Science, Shenzhen Campus of Sun Yat-sen University, Shenzhen 518107, People's Republic of China

In recent years, topology has offered an elegant degree of freedom (DOF) for light and sound manipulation. There exists persistent effort to explore the origin of topological phases based on symmetry, while it becomes rather challenging in complex networks or multiple DOF systems where geometric symmetries are not apparent. Here, we demonstrate a linear degeneracy induced by latent mirror symmetry in a zigzag granular chain whose DOF is three times larger than its bead number. An isospectral reduction approach and graphical representation are developed to track the topological origin of the degeneracy. We show how the latent mirror symmetry leads to the degeneracy and how it is manifested in a properly chosen eigenmode space. Moreover, we reveal the existence of topological edge states and their robustness against different disorders when the degeneracy is gapped. Our study takes a pivotal step toward exploiting topological waves in complex networks or disordered systems, opening up the perspective of offering new flexibilities for classical wave tailoring.

Topology characterized by an integer called topological invariant is a global feature of an object that cannot be changed continuously. This property, offering the intrinsic robustness of the object against deformations [1,2], soon attracts tremendous attention in modern physics [3–6]. It is found that the band structure of materials/metamaterials can exhibit nontrivial topological phases, allowing for various intriguing transports of topological insulators (TIs) in different wave systems [7–14]. Ruled by the symmetry-related topological invariant, the hallmark of TIs is topological wave propagation on the boundaries that is robust against disorders and defects [15,16]. Examples include time-reversal broken structures exhibiting the quantum Hall effect [17], Z_2 topological structures with spin/pseudospin displaying the quantum spin Hall effect [18], and Hexagonal lattices supporting quantum valley-Hall effect [19]. Moreover, higher-order TIs also have been successfully demonstrated in 2D and 3D topological systems that support 0D corner states [20–24]. In addition, numerous studies have been carried out to investigate the topological characteristics in non-Hermitian [25], nonlinear [26], and non-Abelian systems [27]. These recent developments of TIs lead to potential applications in quantum electronics, photonics, acoustics, mechanics, quantum computing, and sensing [28–31].

Since the robustness features arising from the band topology usually are linked to symmetry, it is at the heart of TIs to seek the topological origin through symmetry analysis [32,33]. It has been shown that topological phases of matter can be classified into different categories using time-reversal, particle-hole, and chiral symmetry [34,35]. In addition, geometrical symmetries such as the molecular point group in chemistry [36] or the space group in crystallography [37] have also been shown to exhibit intriguing topological con-

sequences. For instance, the topological crystalline insulators are the counterpart of TIs that have metallic surface states with band degeneracy on high symmetry crystal surfaces [38]. However, in aperiodic/noncrystalline systems or structures with many DOFs, to identify the topological origin becomes challenging. Such systems usually have no physically meaningful symmetry group, but accidental degeneracies of eigenenergies somehow happen to coincide at some locations in the parameter space [39], allowing for nontrivial topological phases. Examples can be found in complex networks [40] and amorphous systems [41,42], in both of which cases topological waves are observed even though the protection mechanism is unclear.

Recently, latent symmetry has been revealed to be an interesting local property in graph theory [43]. The so-called latent symmetry is a generalization of network (graph) symmetry that is defined in a reduced version of the network. Interestingly, latent symmetry has been shown to have the abilities to induce band degeneracy in complex physical systems [44,45]. In this Letter, we report the topology outcome of a linear degeneracy induced by a latent mirror symmetry in a zigzag granular chain (ZGC). We introduce an isospectral reduction approach to unearth the hidden symmetry after a suitable dimensional reduction of the system Hamiltonian while preserving the eigenspectra. This approach allows us to characterize the hidden topological invariant in the reduced subspace. Finally, we show the existence of novel topological edge states induced by the latent mirror symmetry when the degeneracy is gapped. The robustness of said edge states against different disorders is demonstrated.

The ZGC is shown in Fig. 1(a) where elastic beads in contact are placed in a zigzag arrangement (the relative angle between the direction passing through the centers of two adjacent beads to the x axis is $\pi/6$). We consider out-of-plane motion, that is, each bead in the ZGC has three DOFs including one displacement u along the z-axis and two rotations Φ, Ψ along x and y axes [orange dashed box in Fig. 1(a)],

―――――――
[*]zhengly27@mail.sysu.edu.cn
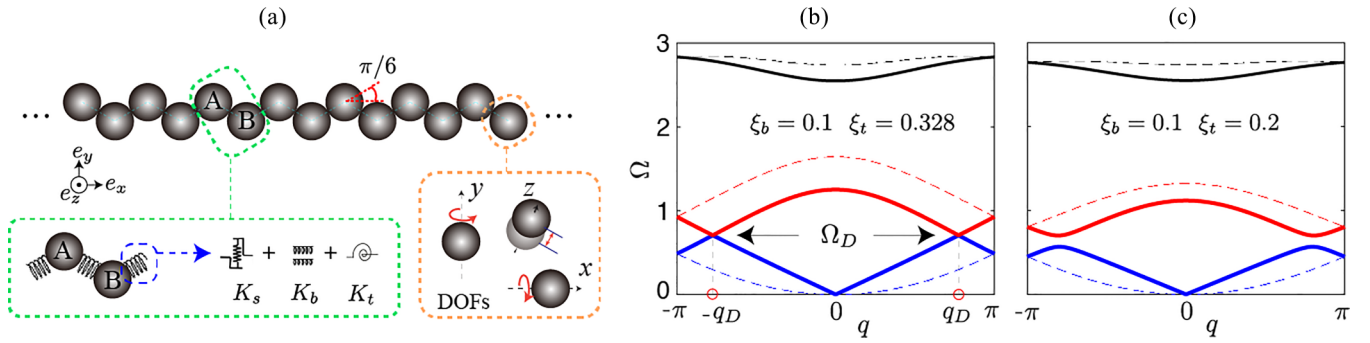[†]huangysh59@mail.sysu.edu.cn

FIG. 1. Schematic presentation of the zigzag granular chain and its band structures. (a) A unit cell marked by a green dashed box contains two sublattice beads A and B. Each bead has two rotational DOFs along the x and y axes, respectively, and one translational DOF along the z axis. The interactions between beads are characterized by effective springs with shear K_s, bending K_b, and torsional K_t rigidities. (b) and (c) show the bulk band structures with dashed lines representing $\mathcal{H}_e$ modes and solid lines corresponding to $\mathcal{H}_o$ modes. (b) $\xi_b = K_b/K_s = 0.1$ and $\xi_t = K_t/K_s = 0.328$. The latent symmetry induced linear degeneracies appear at $\pm q_D$. (c) For $\xi_b = 0.1$ and $\xi_t = 0.2$, the degeneracy is gapped.

and there are shear, bending, and torsional interactions between neighboring beads. A unit cell with two sublattices A, B and six DOFs in total is shown in Fig. 1(a) (green dashed box). The wave dynamics in the ZGC can be theoretically analyzed [18,46], and be further decoupled into two subsystems due to sublattice symmetry [see the Supplemental Material (SM)[47]],

$$\Omega^2 \begin{pmatrix} U_e \\ U_o \end{pmatrix} = \begin{pmatrix} \mathcal{H}_e & 0 \\ 0 & \mathcal{H}_o \end{pmatrix} \begin{pmatrix} U_e \\ U_o \end{pmatrix}, \tag{1}$$

where $U_j = [u_j; \Phi_j; \Psi_j] = (U_A - s_j U_B)/\sqrt{2}$ with the subscript $j = \{e, o\}$, the sign factor $s_{e/o} = \mp$. $U_{A/B}$ is the vector containing the three DOFs of bead A/B. Ω is a normalized frequency. The Hamiltonian of each subsystem reads

$$\mathcal{H}_j(q, \xi_b, \xi_t) = \begin{pmatrix} f_j & a_j & ib_j \\ a_j & g_j & ic_j \\ -ib_j & -ic_j & h_j \end{pmatrix}. \tag{2}$$

Above, $\xi_{b,t} = \frac{K_{b,t}}{K_s}$ is the normalized bending/torsional rigidity, and $q \in [-\pi, \pi]$ is the normalized wave vector. The expression of matrix elements can be found in the SM. The band structures for $\xi_b = 0.1$, $\xi_t = 0.328$, and $\xi_b = 0.1$, $\xi_t = 0.2$ are shown in Figs. 1(b) and 1(c), respectively. One can see that in both (b) and (c), three linear degeneracies of the same origin (overlapping of the $\mathcal{H}_e$ modes with the $\mathcal{H}_o$ ones) appear at $q = \pm\pi$. However in Fig. 1(b), there exists a different type of linear degeneracy only for the $\mathcal{H}_o$ modes at $\pm q_D$. As discussed in the following, this degeneracy is protected by a latent mirror symmetry that can give rise to novel topological states with robustness against disorders.

The latent symmetry in the ZGC, reflecting the local properties of its eigenmodes around $\pm q_D$, is usually hidden in the Hamiltonian $\mathcal{H}_j$. We begin with the graphical representation of $\mathcal{H}_j$ depicted in Fig. 2(a). Three pure modes u_j, Φ_j, Ψ_j in the subspace U_j are highlighted by circles with different colors, and their interactions are marked by lines with arrows denoting the coupling directions. The graph symmetry (if any) corresponds to the Hamiltonian's symmetry that can be analyzed in its graphical representation. Though it is difficult to

identify symmetry in Fig. 2(a), this becomes possible by importing an isospectral reduction (IR) approach which reduces the dimension of $\mathcal{H}_j$ but preserves the eigenvalue spectrum [44,45],

$$\mathcal{R}_{S_j} = \mathcal{H}_{S_j S_j} - \mathcal{H}_{S_j \bar{S}_j} \left(\mathcal{H}_{\bar{S}_j \bar{S}_j} - \Omega^2 I \right)^{-1} \mathcal{H}_{\bar{S}_j S_j}. \tag{3}$$

S_j is a set of modes in U_j, and $\bar{S}_j$ its complementary set. $\mathcal{H}_{S_j S_j}$ and $\mathcal{H}_{\bar{S}_j \bar{S}_j}$ denote the respective Hamiltonians of the subsystems consisting modes only in S_j or $\bar{S}_j$. $\mathcal{H}_{S_j \bar{S}_j}$ and $\mathcal{H}_{\bar{S}_j S_j}$ represent the couplings between the two subsystems. Thus, $\mathcal{R}_{S_j}$ can be regarded as an effective Hamiltonian gained from a subsystem partitioning of $\mathcal{H}_j$. If there exists a symmetry Σ over S_j satisfying $[\mathcal{R}_{S_j}, \Sigma] = 0$ for all Ω, then the original Hamiltonian $\mathcal{H}_j$ has latent symmetry on S_j. For instance, by choosing $S_j = \{\Phi_j, \Psi_j\}$ and $\bar{S}_j = \{u_j\}$, we have

$$\mathcal{R}_{S_j} = m_j \sigma_0 + m_j \left(\frac{\rho_j}{m_j} \sigma_y + \frac{\delta_j}{m_j} \sigma_z \right), \tag{4}$$

whereby $m_j = \frac{g_j + h_j}{2} - \frac{a_j^2 + b_j^2}{2(f_j - \Omega^2)}$, $\rho_j = \frac{a_j b_j}{f_j - \Omega^2} - c_j$, and $\delta_j = \frac{g_j - h_j}{2} - \frac{a_j^2 - b_j^2}{2(f_j - \Omega^2)}$. σ_0 is a 2×2 identity matrix, and $\sigma_{x,y,z}$ are Pauli matrices. The first term in Eq. (4) is trivial and can be ignored. The second and third terms anticommute with the chiral symmetry σ_x. In other words, since $\mathcal{R}_{S_j} - m_j \sigma_0$ is σ_x chiral for all Ω, its eigenmodes (same as $\mathcal{R}_{S_j}$) must be chiral as well, then the original eigenmodes in U_j must be locally σ_x chiral on S_j. To have a degeneracy of the chiral mode pair, additional mirror symmetry is required. According to Eq. (4) and its graph in Fig. 2(b), a mirror line vertically placed in the middle of Φ_j and Ψ_j appears when $\rho_j = \delta_j = 0$. By setting $\xi_b = 0.1$, $\xi_t = 0.328$, we show the changes of Ω as functions of q for $\rho_o = 0$ (cyan line), and $\delta_o = 0$ (magenta line) in Fig. 2(c), respectively. The curves for $\rho_e = 0$ and $\delta_e = 0$ do not intersect, see the SM. Unsurprisingly, the intersection of the two lines overlaps perfectly with the degenerate points (gray lines) at Ω_D as expected, conforming our prediction.

It should point out that the local properties of the eigenmodes in the ZGC might be manifested directly in the isomorphic matrix graph of $\mathcal{H}_j$, but this requires the transformation of mode basis that is usually hard to achieve. In our
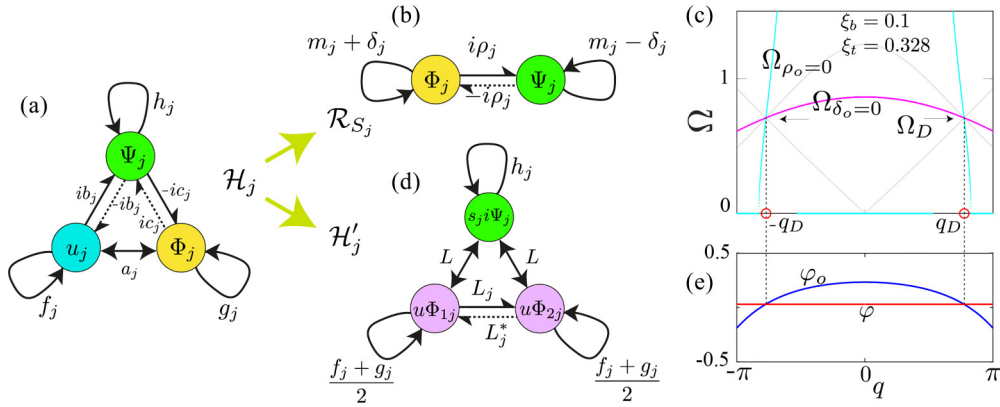
FIG. 2. Graphical representations for $\mathcal{H}_j$, $\mathcal{R}_{S_j}$, and $\mathcal{H}'_j$. The colored circles represent different pure modes in the corresponding eigenmode space. Arrowed lines stand for the couplings between modes, and loops starting and ending at the same circles mark the on-site potentials. (a) Graph of $\mathcal{H}_j$. (b) σ_x chiral is visualized and a mirror placed vertically in between the two circles is possible when $\delta_j = \rho_j = 0$. (c) The lines of $\delta_o = 0$ and $\rho_o = 0$ cross each other at $\pm q_D$ where the degeneracies appear (gray lines). (d) A mirror passing vertically through the green circle exists when $\mathrm{Im}(L_j) = 0$. This requires $\varphi_j - \varphi = 0$. (e) The curves of φ_o and φ for $q \in [-\pi, \pi]$ intersect at $\pm q_D$.

case, under the basis $\boldsymbol{U}'_j = \mathcal{Y}_j \boldsymbol{U}_j$ (see the form of $\mathcal{Y}_j$ in the SM), the new Hamiltonian reads

$$\mathcal{H}'_j = \begin{pmatrix} \frac{f_j + g_j}{2} & L_j & L \\ L_j^* & \frac{f_j + g_j}{2} & L \\ L & L & h_j \end{pmatrix}, \qquad (5)$$

where $L_j = \frac{\sqrt{4a_j^2 + (f_j - g_j)^2}}{2} e^{-i(\varphi_j - \varphi)}$, $L = \sqrt{\frac{b_j^2 + c_j^2}{2}}$ with $\varphi_j = \arctan\frac{f_j - g_j}{2a_j}$ and $\varphi = 2\arctan\frac{b_j - c_j}{b_j + c_j}$ (the values of L and φ do not change for $j = e$ or $j = o$). The corresponding dynamical graph is shown in Fig. 2(d), where a mirror line passing vertically through the center of the green circle (pure $s_j i \Psi_j$ mode) exhibits as long as $\mathrm{Im}(L_j) = 0$, that is, the condition $\varphi_j - \varphi = 0$ is satisfied. Similarly, this condition can be ful-

filled only in the $\boldsymbol{U}_o$ subspace, while it cannot in $\boldsymbol{U}_e$, see the SM. The changes of φ_o (blue line) and φ (red line) as functions of q are shown in Fig. 2(e), respectively. A good agreement with the IR analysis is witnessed as the two lines cross each other when $q = \pm q_D$. Thus, we conclude that the mirror line reflecting the local properties of the $\boldsymbol{U}_o$ modes around $\pm q_D$ is the hidden symmetry that becomes evident in the subspace $\boldsymbol{U}'_o$.

The latent-mirror-induced degeneracy can lead to novel topological edge states on the boundaries of the ZGC when gapped. By fixing $\xi_b = 0.1$, we found that the change of ξ_t from larger to smaller values than 0.328 results in the closing (trivial) and reopening (nontrivial) of a band gap companioning with the topological phase transition at $\xi_t = 0.328$. Figures 3(a) and 3(b) show the dispersion curves (red dots)
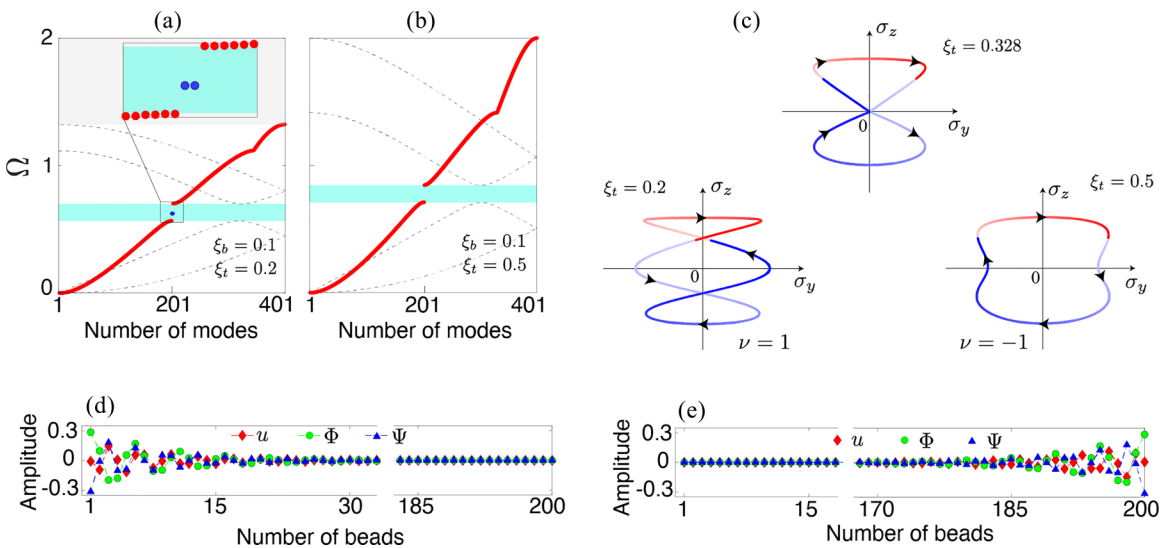

FIG. 3. Eigenfrequency calculations of a ZGC consisting of 200 beads with free boundaries. (a) The setting $\xi_b = 0.1$, $\xi_t = 0.2$ corresponds to the topological phase. Red/blue dots label the bulk/edge modes. Cyan area is the band gap. Bulk band structure is also presented by gray dashed lines. (b) The setting $\xi_b = 0.1$, $\xi_t = 0.5$ belongs to the trivial phase. No edge states are observed inside the band gap. (c) The winding of $\mathcal{R}_{S_j}$. Red/blue lines correspond to the occupied S_e / S_o bands. The color level from light to dark indicates the value of q varying from $[-\pi, \pi]$. (d) and (e) show the profiles of the eigenmodes of the edge states in (a).

of a ZGC consisting of 200 beads with free boundaries for $\xi_t = 0.2$ and $\xi_t = 0.5$, respectively. The corresponding band structures from $\mathcal{H}_j$ (gray dashed curves) are also displayed in the background. Though both cases exhibit a bang gap (cyan), the one in (a) is topologically nontrivial with two topological edge states (blue dots in the zoomed view) appearing in the band gap. Regarding $\mathcal{R}_{S_j}$ as an effective Hamiltonian, it is possible to characterize the band topology around its "zero energy" (i.e., Ω_D for $\mathcal{H}_j$) since $\mathcal{R}_{S_j}$ has the symmetry σ_x although $\mathcal{H}_j$ does not. We define the winding of $\mathcal{R}_{S_j}$ through the skew polarization [48],

$$P = \frac{1}{2\pi} \oint dq \mathcal{A}(q), \quad \mathcal{A}(q) = i \sum_{l \in \text{occ}} \langle \sigma_x \psi_l | \partial_q | \psi_l \rangle. \quad (6)$$

Above, occ denotes the two occupied bands (one from $\mathcal{R}_{S_e}$, the other from $\mathcal{R}_{S_o}$). P is quantized in units of $1/2$ and it connects to the winding number by $2P = \nu \mod 2$. Therefore, $\nu(\xi_t < 0.328) = 1$ and $\nu(\xi_t > 0.328) = -1$ with a phase transition at $\xi_t = 0.328$ when P switches its sign, see the SM. In fact, the winding also can be seen from the σ_y-σ_z plane in Fig. 3(c) where the trajectories of $(\frac{\rho_j}{m_j}, \frac{\delta_j}{m_j})$ winding around the origin counterclockwise ($\xi_t = 0.2$) or clockwise ($\xi_t = 0.5$) are displayed. The net winding number, which accounts for the difference in winding from $\xi_t < 0.328$ to $\xi_t > 0.328$, can be defined as $\Delta\nu = \nu(\xi_t < 0.328) - \nu(\xi_t > 0.328) = 2$. The band topology enforces the bulk-edge correspondence: $|\Delta\nu|$, which denotes the number of edge states at the end of the ZGC. The eigenprofiles of the two edge states are presented in Figs. 3(d) and 3(e). Two important features are observed. First, the displacements (red markers) and rotations (green and blue markers) of both sublattices A, B contribute to the eigenprofiles. Second, the edge states appear on both ends of the chain, indicating their existence does not depend on the termination configuration of sublattice type. These features make the topological edge states very different from those reported in the SSH model, in which only one type of sublattice contributes to the edge states, and the existence of edge states relies on a specific sublattice configuration in the end of the chain [49].

Another intriguing property about the aforementioned topological edge states is the robustness against different disorders. In Fig. 4(a), we consider the same ZGC configuration as Fig. 3(a), but now with the beads of random masses that are uniformly distributed in $[(1 - \gamma_M)M, (1 + \gamma_M)M]$ where M is the unperturbed mass in Fig. 3(a). For each $\gamma_M \in [0, 0.2]$, we calculate the eigenfrequency spectra over 200 ZGC configurations with disorders, and mark the eigenfrequencies by dots. Finally, the distribution of eigenmodes in the (Ω, γ_M) space is obtained in Fig. 4(a), where the red/gray areas mark the regions of the edge/bulk modes. It can be seen that with up to a 20% variation on the bead mass, we still can obtain the topological edge states in the ZGC. In Fig. 4(b), we keep
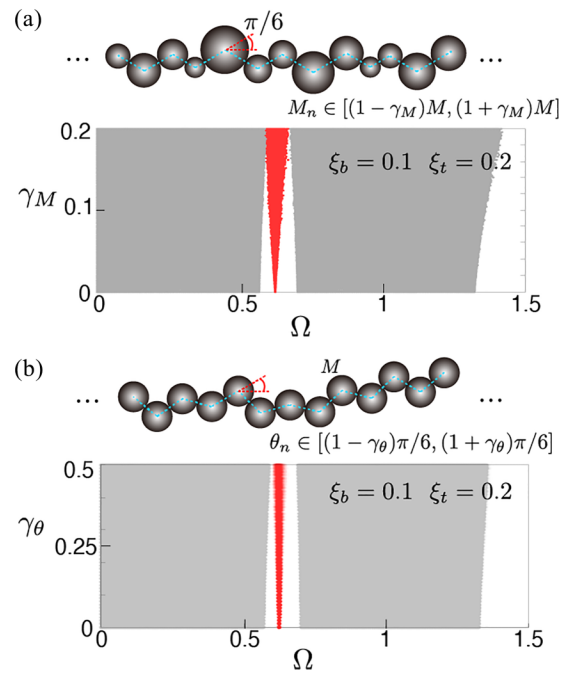

FIG. 4. Robustness verifications of topological edge states under different disorder settings. (a) Distribution of eigenfrequency for random mass in $[(1 - \gamma_M)M, (1 + \gamma_M)M]$ over 200 ZGC configurations for each γ_M. Gray/red dots mark the positions of bulk/edge states. (b) Same as (a) but with identical mass in the chain while the angles of every two beads are randomly distributed in $[(1 - \gamma_\theta)\pi/6, (1 + \gamma_\theta)\pi/6]$.

the mass of beads unchanged, now the angle between two adjacent beads is no longer $\pi/6$ but uniformly distributed in $[(1 - \gamma_\theta)\pi/6, (1 + \gamma_\theta)\pi/6]$. Similarly, for each $\gamma_\theta \in [0, 0.5]$, we calculate the eigenfrequency spectra over 200 ZGC configurations, and the distribution of eigenfrequencies in the (Ω, γ_θ) space is shown in Fig. 4(b). As expected, the topological edge states are very robust and persist to appear in the band gap, even though up to a 50% variation on the angle between beads is imposed.

In conclusion, we have demonstrated a latent-mirror-induced degeneracy in a granular chain that can lead to novel topological edge states when appropriately gapped. An isospectral reduction approach and graphical representation have been developed to unveil the existence of the latent symmetry in the eigenstate subspace. We have exposed the topological edge states, demonstrating their robustness against various disorders. We foresee that our study can trigger the exploration of topological waves in different multiple DOF systems and disordered settings.

[1] M. Z. Hasan and C. L. Kane, Rev. Mod. Phys. **82**, 3045 (2010).

[2] X.-L. Qi and S.-C. Zhang, Rev. Mod. Phys. **83**, 1057 (2011).

[3] T. Ozawa, H. M. Price, A. Amo, N. Goldman, M. Hafezi, L. Lu, M. C. Rechtsman, D. Schuster, J. Simon, O. Zilberberg *et al.*, Rev. Mod. Phys. **91**, 015006 (2019).

[4] H. Xue, Y. Yang, and B. Zhang, Nat. Rev. Mater. **7**, 974 (2022).

[5] X. Ni, S. Yves, A. Krasnok, and A. Alù, Chem. Rev. (2023).

[6] X. Zhang, F. Zangeneh-Nejad, Z.-G. Chen, M.-H. Lu, and J. Christensen, Nature (London) **618**, 687 (2023).

[7] C. L. Kane and E. J. Mele, Phys. Rev. Lett. **95**, 226801 (2005).

[8] L. Fu and C. L. Kane, Phys. Rev. B **76**, 045302 (2007).

[9] A. B. Khanikaev, S. Hossein Mousavi, W.-K. Tse, M. Kargarian, A. H. MacDonald, and G. Shvets, Nat. Mater. **12**, 233 (2013).

[10] Y. Yang, Z. Gao, H. Xue, L. Zhang, M. He, Z. Yang, R. Singh, Y. Chong, B. Zhang, and H. Chen, Nature (London) **565**, 622 (2019).

[11] W.-J. Chen, S.-J. Jiang, X.-D. Chen, B. Zhu, L. Zhou, J.-W. Dong, and C. T. Chan, Nat. Commun. **5**, 5782 (2014).

[12] C. He, X. Ni, H. Ge, X.-C. Sun, Y.-B. Chen, M.-H. Lu, X.-P. Liu, and Y.-F. Chen, Nat. Phys. **12**, 1124 (2016).

[13] S.-Y. Yu, C. He, Z. Wang, F.-K. Liu, X.-C. Sun, Z. Li, H.-Z. Lu, M.-H. Lu, X.-P. Liu, and Y.-F. Chen, Nat. Commun. **9**, 3072 (2018).

[14] S. D. Huber, Nat. Phys. **12**, 621 (2016).

[15] A. Coutant, V. Achilleos, O. Richoux, G. Theocharis, and V. Pagneux, Phys. Rev. B **102**, 214204 (2020).

[16] E. J. Meier, F. A. An, A. Dauphin, M. Maffei, P. Massignan, T. L. Hughes, and B. Gadway, Science **362**, 929 (2018).

[17] F. D. M. Haldane and S. Raghu, Phys. Rev. Lett. **100**, 013904 (2008).

[18] L.-Y. Zheng, G. Theocharis, V. Tournat, and V. Gusev, Phys. Rev. B **97**, 060101(R) (2018).

[19] J. Lu, C. Qiu, M. Ke, and Z. Liu, Phys. Rev. Lett. **116**, 093901 (2016).

[20] L.-Y. Zheng and J. Christensen, Phys. Rev. Lett. **127**, 156401 (2021).

[21] Q. Wei, X. Zhang, W. Deng, J. Lu, X. Huang, M. Yan, G. Chen, Z. Liu, and S. Jia, Phys. Rev. Lett. **127**, 255501 (2021).

[22] F. Schindler, A. M. Cook, M. G. Vergniory, Z. Wang, S. S. Parkin, B. A. Bernevig, and T. Neupert, Sci. Adv. **4**, eaat0346 (2018).

[23] L. Luo, H.-X. Wang, Z.-K. Lin, B. Jiang, Y. Wu, F. Li, and J.-H. Jiang, Nat. Mater. **20**, 794 (2021).

[24] B. Xie, H.-X. Wang, X. Zhang, P. Zhan, J.-H. Jiang, M. Lu, and Y. Chen, Nat. Rev. Phys. **3**, 520 (2021).

[25] B. Hu, Z. Zhang, H. Zhang, L. Zheng, W. Xiong, Z. Yue, X. Wang, J. Xu, Y. Cheng, X. Liu *et al.*, Nature (London) **597**, 655 (2021).

[26] F. Zangeneh-Nejad and R. Fleury, Phys. Rev. Lett. **123**, 053902 (2019).

[27] Z.-G. Chen, R.-Y. Zhang, C. T. Chan, and G. Ma, Nat. Phys. **18**, 179 (2022).

[28] J. C. Budich and E. J. Bergholtz, Phys. Rev. Lett. **125**, 180403 (2020).

[29] A. Blanco-Redondo, B. Bell, D. Oren, B. J. Eggleton, and M. Segev, Science **362**, 568 (2018).

[30] S. Mittal, E. A. Goldschmidt, and M. Hafezi, Nature (London) **561**, 502 (2018).

[31] H. Qiao, É. Dumur, G. Andersson, H. Yan, M.-H. Chou, J. Grebel, C. Conner, Y. Joshi, J. Miller, R. Povey *et al.*, Science **380**, 1030 (2023).

[32] C.-K. Chiu, J. C. Y. Teo, A. P. Schnyder, and S. Ryu, Rev. Mod. Phys. **88**, 035005 (2016).

[33] J. Kruthoff, J. de Boer, J. van Wezel, C. L. Kane, and R.-J. Slager, Phys. Rev. X **7**, 041069 (2017).

[34] S. Ryu, A. P. Schnyder, A. Furusaki, and A. W. Ludwig, New J. Phys. **12**, 065010 (2010).

[35] R. Süsstrunk and S. D. Huber, Proc. Natl. Acad. Sci. USA **113**, E4767 (2016).

[36] B. Bradlyn, L. Elcoro, J. Cano, M. G. Vergniory, Z. Wang, C. Felser, M. I. Aroyo, and B. A. Bernevig, Nature (London) **547**, 298 (2017).

[37] H. C. Po, A. Vishwanath, and H. Watanabe, Nat. Commun. **8**, 50 (2017).

[38] L. Fu, Phys. Rev. Lett. **106**, 106802 (2011).

[39] D. R. Yarkony, Rev. Mod. Phys. **68**, 985 (1996).

[40] Z. Zhang, P. Delplace, and R. Fleury, Sci. Adv. **9**, eadg3186 (2023).

[41] A. Agarwala and V. B. Shenoy, Phys. Rev. Lett. **118**, 236402 (2017).

[42] Y. Long, J. Ren, and H. Chen, Phys. Rev. Lett. **124**, 185501 (2020).

[43] D. Smith and B. Webb, Physica A **514**, 855 (2019).

[44] M. Röntgen, M. Pyzh, C. Morfonios, N. Palaiodimopoulos, F. Diakonos, and P. Schmelcher, Phys. Rev. Lett. **126**, 180601 (2021).

[45] M. Röntgen, C. V. Morfonios, P. Schmelcher, and V. Pagneux, Phys. Rev. Lett. **130**, 077201 (2023).

[46] L.-Y. Zheng, F. Allein, V. Tournat, V. Gusev, and G. Theocharis, Phys. Rev. B **99**, 184113 (2019).

[47] See Supplemental Material at http://link.aps.org/supplemental/10.1103/PhysRevB.108.L220303 for details about (i) theoretical model, (ii) isospectral reduction, (iii) band inversion, (iv) topological index, and (v) eigenprofiles of edge state with disorders.

[48] I. Mondragon-Shem, T. L. Hughes, J. Song, and E. Prodan, Phys. Rev. Lett. **113**, 046802 (2014).

[49] J. K. Asbóth, L. Oroszlány, and A. Pályi, *A Short Course on Topological Insulators: Band Structure and Edge States in One and Two Dimensions* (Springer, Cham, 2016).